JOURNAL OF GEOPHYSICAL RESEARCH, VOL. 101, NO. D10, PAGES 14,999–15,012, JUNE 27, 1996

Radiative effects of convection in the tropical Pacific

W.D. Collins,[1,2] F.P.J. Valero,[2,3] P.J. Flatau,[2] D. Lubin,[1,2]
H. Grassl,[4,5] and P. Pilewskie[6]

Abstract. The radiative effects of tropical clouds at the tropopause and the ocean surface have been estimated by using *in situ* measurements from the Central Equatorial Pacific Experiment (CEPEX). The effect of clouds is distinguished from the radiative effects of the surrounding atmosphere by calculating the shortwave and longwave cloud forcing. These terms give the reduction in insolation and the increase in absorption of terrestrial thermal emission associated with clouds. At the tropopause the shortwave and longwave cloud forcing are nearly equal and opposite, even on daily timescales. Therefore the net effect of an ensemble of convective clouds is small compared to other radiative terms in the surface-tropospheric heat budget. This confirms the statistical cancellation of cloud forcing observed in Earth radiation budget measurements from satellites. At the surface the net effect of clouds is to reduce the radiant energy absorbed by the ocean. Under deep convective clouds the diurnally averaged reduction exceeds 150 W m^{-2}. The divergence of flux in the cloudy atmosphere can be estimated from the difference in cloud forcing at the surface and tropopause. The CEPEX observations show that the atmospheric cloud forcing is nearly equal and opposite to the surface forcing. Based upon the frequency of convection, the atmospheric forcing approaches 100 W m^{-2} when the surface temperature is 303 K. The cloud forcing is closely related to the frequency of convective cloud systems. This relation is used in conjunction with cloud population statistics derived from satellite to calculate the change in surface cloud forcing with sea surface temperature. The net radiative cooling of the surface by clouds increases at a rate of 20 W $m^{-2}K^{-1}$during the CEPEX observing period.

1. Introduction

Clouds have a major influence on the radiation field of the Earth. The radiative effect of clouds is an important component of the Earth's radiation budget and is one of the major sources of uncertainty in climate modeling [*Hartmann et al.*, 1986; *Ramanathan*, 1987; *Webster and Stephens*, 1984]. At the top of the atmosphere, clouds reflect incoming sunlight back to space, thereby reducing the amount of insolation reaching the surface. Clouds also strongly absorb the thermal radiation emitted by the surface and the atmosphere and reduce the amount of heat radiated to space. At the surface, clouds generally reduce the amount of insolation by reflecting and, to some extent, absorbing the incoming sunlight. However, the clouds also act as a source of thermal radiation, and the heat emitted by clouds is added to the downward thermal emission from the clear atmosphere. The effects of clouds in the tropics are of particular importance to the climate system.

[1]Center for Clouds, Chemistry, and Climate, Scripps Institution of Oceanography, University of California, San Diego, La Jolla, California.
[2]California Space Institute, Scripps Institution of Oceanography, University of California, San Diego, La Jolla, California.
[3]Atmospheric Research Laboratory, Scripps Institution of Oceanography, University of California, San Diego, La Jolla, California.
[4,5]Max Planck Institute for Meteorology, Hamburg, Germany and WCRP-WMO, Geneva
[6]NASA Ames Research Center, Moffett Field, California.

Paper number 95JD02534.
0148-0227/96/95JD-02534$09.00

There has been tremendous progress in the last 20 years in estimating the radiative effects of clouds from intensive satellite observations. One of the best data sets has been collected by the Earth Radiation Budget Experiment (ERBE) [*Barkstrom*, 1984; *Barkstrom and Smith*, 1986]. The measurements from ERBE are sufficient to calculate the impact of clouds on the radiation field at the top of the atmosphere to within 10 W m^{-2} [*Harrison et al.*, 1990]. However, progress in estimating the impact of clouds on the radiation at the Earth's surface is limited by the sparse and inhomogeneously distributed network of surface radiometers. This problem is especially acute for the tropical oceans, and many of the existing radiation data sets are collected from instruments on islands. There has been considerable effort devoted to estimating the surface energy budget from a combination of satellite measurements [e.g., *Gupta et al.*, 1993]. The accuracy of the retrieved budget parameters is limited by approximations in the treatment of radiative transfer, systematic errors in the input cloud parameters, and uncertainties in the distribution of radiatively active atmospheric constituents. Further advances in the treatment of tropical convection require *in situ* measurements of the radiative and nonradiative effects of clouds.

Recent field experiments in the tropical Pacific have provided extensive measurements of the surface radiation field. The Tropical Ocean Global Atmosphere Coupled Ocean-Atmosphere Response Experiment (TOGA COARE) was conducted in the western equatorial Pacific from November 1992 through February 1993 [*Webster and Lukas*, 1992]. The Central Equatorial Pacific Experiment (CEPEX) was conducted during March and April 1993 [*Ramanathan et al.*, 1993]. The combined data sets from these experiments contain 5 months of intensive surface observations that extend from the warm pool to the convectively sup-

pressed eastern Pacific. Using data from a TOGA COARE pilot project, *Young et al.* [1992] have shown that deep precipitating convection significantly alters several components of the surface energy budget. Most of the variability in the energy budget is associated with effects of cloud shading. In this paper we evaluate data collected during CEPEX. We have analyzed radiometric measurements at the surface and tropopause to estimate the effect of convective clouds on the total column, the surface, and the atmosphere.

The radiative effects of clouds may be quantified by calculating the shortwave and longwave cloud forcing [*Charlock and Ramanathan*, 1985; *Hartmann et al.*, 1986; *Ramanathan*, 1987]. The cloud forcing is defined as the difference in net radiative flux between clear and average (cloudy) conditions. The shortwave and longwave cloud forcing are given by

$$C_l = F - F_a, \tag{1}$$

$$C_s = S - S_a, \tag{2}$$

where

$$F_a = F_a^+ - F_a^-, \tag{3}$$

$$F = F^+ - F^-, \tag{4}$$

$$S_a = S_a^+ - S_a^-, \tag{5}$$

$$S = S^+ - S^-. \tag{6}$$

Here F_a and F are the net clear-sky and cloudy longwave fluxes, and S_a and S are the corresponding net shortwave fluxes. The individual upwelling and downwelling components of these fluxes are denoted with the superscripts plus and minus, respectively. Typically, $C_s < 0$, since clouds increase the albedo and reduce the downwelling solar radiation. However, $C_l > 0$, because clouds absorb upwelling infrared radiation and emit radiation at lower temperatures than the atmosphere and surface below. The net cloud forcing is defined by

$$C_{net} = C_l + C_s. \tag{7}$$

When $C_{net} < 0$, the clouds reduce the flux into the ocean-atmosphere system. Let $C_l(0)$ and $C_s(0)$ denote the longwave and shortwave cloud forcing at the surface, respectively, and $C_l(\text{Trop})$ and $C_s(\text{Trop})$ denote the corresponding quantities at the tropopause. The atmospheric cloud forcing is the radiative flux absorbed in a cloudy atmosphere and is given by $C_l(A) = C_l(\text{Trop}) - C_l(0)$ and $C_s(A) = C_s(\text{Trop}) - C_s(0)$.

The basic objectives of this paper are to derive the daily mean cloud forcing from *in situ* measurements and to estimate the cloud forcing on the scale of synoptic disturbances. The vertical distribution of cloud forcing is also examined. For tropical convective regions, results from ERBE show that $C_l(\text{Trop}) \approx -C_s(\text{Trop})$ on monthly and seasonal time scales [*Ramanathan et al.*, 1989; *Harrison et al.*, 1990; *Kiehl and Ramanathan*, 1990]. The cancellation implies that the integrated effect of clouds on the ocean-atmospheric column is small. However, theoretical studies of the tropical atmosphere have shown that the surface cloud forcing may be decoupled from the forcing at the top of the atmosphere (TOA) [*Stephens and Webster*, 1984]. Because of the infrared opacity and temperature profile of the tropical atmosphere, $C_l(0)$ depends strongly on the cloud base temperature, while $C_l(\text{Trop})$ is determined by the cloud top temperature and the lapse rate [*Ramanathan*, 1977]. Therefore the relationship of $C_l(0)$ and $C_l(\text{Trop})$ is governed by the vertical distribution of clouds in the atmosphere. For tropical deep convection, modeling studies [*Slingo and Slingo*, 1988; *Harshvardhan et al.*, 1990] and CEPEX observations (W.D. Collins et al., manuscript in preparation, 1995) have shown that $C_l(0) \ll C_l(\text{Trop})$. This implies that the cloud forcing has a dipole structure, with $C_{net}(0) \ll 0$ and $C_{net}(A) \gg 0$ [*Ramanathan et al.*, 1989]. The relationship of $C_{net}(0)$, $C_{net}(A)$, and $C_{net}(\text{Trop})$ is derived from the observations.

In section 2 the instruments and platforms used to collect the radiometric data are described. In addition, the procedures for estimating the terms for clear and cloudy conditions in equations (1) and (2) are derived. In section 3 the cloud forcing is calculated from the measurements. The surface and tropopause values are combined to give a lower bound on the radiative flux divergence in deep convection. In section 4 the measurements are integrated with cloud population statistics obtained from satellite data to generalize the results and compute regional energy budgets. The implications of these findings for further investigations of tropical climate are discussed in section 5.

2. Data and Methods

2.1. *In Situ* and Derived Data

The observations used in this analysis were collected in the central and eastern equatorial Pacific during March and April 1993. The radiometric fluxes at the tropopause were detected with instruments on the NASA ER-2 between 18 and 20 km. The surface fluxes were measured with instruments on a Lockheed P-3 turboprop aircraft operated by the National Oceanic and Atmospheric Administration (NOAA) and on the ship R/V *John Vickers*. A detailed description of the location and times of the aircraft and ship observations is given by *Williams* [1993]. Logistical considerations did not permit many collocated measurements at the surface and tropopause. However, an equatorial track at 2°S extending from 170°E to 170°W was repeatedly sampled from the ER-2 and P-3 during the CEPEX observing period. The R/V *Vickers* traversed the same region from west to east as it sailed from Honiara to Los Angeles.

The ER-2 was equipped with a radiation measurement system (RAMS) and with a cloud detection lidar. The upwelling and downwelling shortwave fluxes S^+ and S^- are measured with a broad spectral bandpass hemispherical field-of-view solar radiometer [*Valero et al.*, 1982, 1984]. The bandpass of this instrument is 0.25 to 2.8 μm. The albedo of the surface-troposphere system is given by $\alpha(\text{Trop}) = S^+/S^-$. To a good approximation the downwelling solar flux is given by $S^- = S_0 \cos(\theta)$, where S_0 is the solar constant and θ is the solar zenith angle. The upwelling longwave flux F^+ is measured by a similar instrument for infrared wavelengths between 4 and 40 μm. The flux measurements are accurate to better than 1%. In calculating $C_l(\text{Trop})$ we neglect the contribution of the downwelling flux from the stratosphere, since it is not expected to vary significantly from clear to cloudy conditions. The upwelling radiance in the midinfrared window at 10.5 μm is used in conjunction with the cloud detection lidar [*Spinhirne and Hart*, 1990] to estimate the upwelling clear-sky shortwave flux. Data from two flights on March 20 and April 3, 1993 are not included in the analysis owing to instrument malfunction.

The downwelling solar flux at the ocean surface was measured with an Eppley pyranometer on the R/V *Vickers*. The spectral bandpass of the pyranometer is 0.295 to 2.8 μm. The down-

welling infrared flux is calculated from the downwelling infrared radiance field. The zenith radiance was measured with a Fourier transform infrared (FTIR) spectroradiometer. The radiances are recorded with 1 cm^{-1} resolution over the wavenumber interval 500-2000 cm^{-1} by using a narrow field-of-view detector aligned with the local zenith. The integrated downwelling flux in this spectral interval is estimated by using limb-darkening models derived from coincident high-resolution atmospheric soundings [*Lubin et al.*, 1995]. The worst-case uncertainty in the flux estimates from errors in absolute radiometric calibration is approximately ±6 W m^{-2}. Infrared absorption bands outside the spectral bandpass of the FTIR are virtually saturated in the tropical atmosphere. As a result the contribution to $C_l(0)$ from wavenumbers outside the FTIR bandpass may be neglected, (W.D. Collins et al., manuscript in preparation, 1995).

The shortwave and longwave fluxes within 33 m of the ocean surface were measured by using Eppley pyranometers and pyrgeometers on the NOAA P-3. The spectral band pass of the pyranometers is also 0.285 to 2.8 μm, and the bandpass of the pyrgeometers is approximately 5 to 50 μm. The upwelling and downwelling fluxes were measured with pairs of identical Eppley instruments. At the beginning of the CEPEX observation period the pyrgeometers were calibrated against a reference blackbody cavity, and the pyranometers were calibrated against a reference solar radiometer. The fluxes are accurate to within 15 W m^{-2}. A narrowband spectral PRT-5 instrument is used to estimate the sea surface temperature from the upwelling 9.5- to 11.5- μm radiance.

2.2 Estimation of Fluxes for Clear Conditions

The cloud forcing defined by equations (1) and (2) is the difference between the observed net flux and a background clear-sky net flux. In regions with persistent cloud cover it may not be possible to determine the fluxes for clear-sky and cloudy conditions simultaneously. For example, the lidar on the ER-2 aircraft detected clear sky only 6% of the time during 10 research flights. Since the variability in the clear-sky fluxes is much smaller than the variability introduced by clouds, we have developed empirical expressions for estimating the background clear-sky flux under cloudy conditions. The expressions are validated against the limited sample of clear-sky measurements for each platform. This method is similar to one of the approaches used to calculate cloud forcing from GCMs [*Cess and Potter*, 1987; *Cess et al.*, 1992]. The cloud forcing calculated with this approach includes the radiative effects of variations in the water vapor profiles between clear and cloudy regions. Formulas for the clear-sky fluxes have been determined for each of the aircraft and ship radiometers and are presented below.

2.2.1 Clear-sky fluxes at the tropopause. The longwave flux $F_a^+(\text{Trop})$ is related to the atmospheric greenhouse effect by

$$G_a(\text{Trop}) = b\sigma T_s^4 - F_a^+(\text{Trop}), \quad (8)$$

where σ is the Stefan-Boltzmann constant, 5.67 x 10^{-8} W m^{-2} K^{-4}, and b = 0.944 is an adjustment for the spectral bandpass of the longwave radiometer. In the tropics, most of the variability in $G_a(\text{Trop})$ is related to variations in the sea surface temperature T_s and the atmospheric humidity [*Raval and Ramanathan*, 1989; *Inamdar and Ramanathan*, 1994]. The CEPEX observations show that $G_a(\text{Trop})$ increases more rapidly with ocean temperature than does the surface emission [*Weaver et al.*, 1994], an effect known as the supergreenhouse effect [*Ramanathan and Collins*, 1991]. A least squares linear fit to the clear-sky measurements from the ER-2 (F.P.J. Valero et al., manuscript in preparation, 1995) gives

$$G_a(\text{Trop}) = 145.3 + 15.3(T_s - 300) \text{ W m}^{-2}, \quad (9)$$

The regression explains approximately 70% of the variance in the greenhouse absorption. The clear-sky flux $F_a^+(\text{Trop})$ is estimated by combining (8) and the empirical relation (9). The relation of $G_a(\text{Trop})$ to T_s is strongly effected by the distribution of convection during CEPEX, and is not necessarily representative of climatogical conditions.

The clear-sky upwelling solar flux is related to the clear-sky albedo by $S_a^+(\text{Trop}) = S_0\alpha_a(\text{Trop},\theta)$. The clear-sky albedos measured from the ER-2 are shown as a function of solar zenith angle in Figure 1. The clear-sky observations are selected with the same criteria as those used to determine the atmospheric greenhouse effect (F.P.J. Valero et al., manuscript in preparation, 1995), with the additional requirements that the 10.5-μm brightness temperatures exceed 295 K and no clouds are detected by the lidar. The angle of the Sun from the zenith is computed from the position of the aircraft and time of day by using a solar ephemeris [*Michalsky*, 1988; *Spencer*, 1989]. The figure shows two features characteristic of the albedo over clear ocean regions. First, the albedo when the Sun is directly overhead is less than 10%, with minimum values of 6%. Second, the clear-sky albedo is a strong function of solar zenith angle. For moderate angles the albedo is proportional to 1 / cos (θ).

The dependence of clear-sky albedo on sun angle may be approximated by

$$\alpha_a(\text{Trop},\theta) = 0.06\ \delta(\theta), \quad (10)$$

The function $\delta(\theta)$ is the ratio of the TOA albedo to the TOA albedo for overhead Sun. Although a number of factors influence this ratio, including the surface roughness and the aerosol optical depth, the associated changes in $\alpha_a(\text{Trop},\theta)$ and $C_s(\text{Trop})$ are not significant. The directional albedo model from ERBE is used for $\delta(\theta)$ [*Brooks et al.*, 1986; *Suttles*, 1988]. The value of $\alpha_a(\text{Trop},0)$ = 0.06 is determined from the minimum observed albedo for overhead Sun. Since the criteria for selecting clear-sky scenes are necessary but not sufficient conditions to eliminate cloud contamination in the hemispherical albedo, the minimum value of

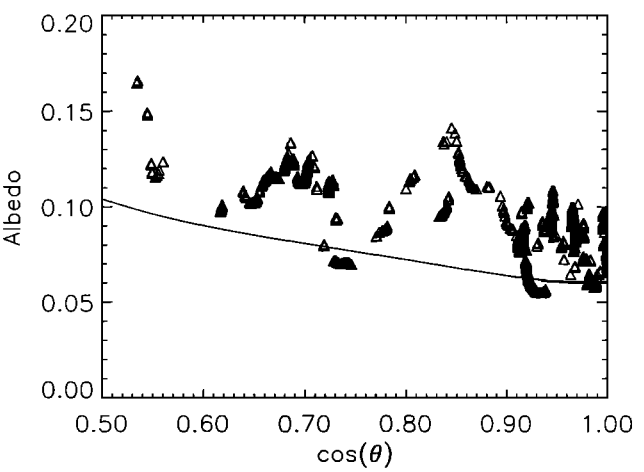

Figure 1. Clear-sky albedo $\alpha_a(\text{Trop},\theta)$ at the tropopause measured from the NASA ER-2 as a function of the cosine of the solar zenith angle. Solid line is the fit to the data given by equation (10).

α_a(Trop,0) consistent with the measurements is used. The clear-sky observations and equation (10) are plotted in Figure 1.

2.2.2 Clear-sky fluxes at the surface. The net shortwave flux $S_a(0)$ under clear conditions is estimated by using the method of *Li and Leighton* [1993]. The parameterization agrees with clear-sky surface fluxes measured during CEPEX to within 10 W m^{-2}. The calculation of $S_a(0)$ depends upon the TOA clear sky albedo, the solar zenith angle, and the column-integrated precipitable water vapor p (in centimeters). The clear sky albedo is calculated by using equation (10), and the zenith angle is computed from the solar ephemeris. For the R/V *Vickers* observations, p is calculated from vertical profiles of temperature and humidity measured with radiosondes [*Weaver et al.*, 1994]. The radiosondes were launched at 6 hour intervals as the ship sailed across the central Pacific. A time series of precipitable water coincident with the surface radiometric data is obtained by linear interpolation. For the P-3 observations the precipitable water is determined from fields of temperature and humidity analyzed by the European Centre for Medium-Range Weather Forcasts (ECMWF). The fields used in this analysis have a temporal resolution of 6 hours and a spatial resolution of 1.1°. At each point along the flight path of the aircraft, p is estimated by using bilinear interpolation from the values of p at the four nearest grid points. Comparison of p derived from the soundings and the analyzed fields shows that the rms error in the ECMWF estimates is $\delta p = 0.63$ cm, or roughly 14% of the mean value of $p = 4.5$ cm. The fractional error in $S_a(0)$ due to the uncertainty δp in p is less than 1% when $\theta = 0°$ and increases to 3% for $\theta = 80°$ [*Li and Leighton*, 1993].

The longwave flux $F_a(0)$ is determined with separate procedures for the FTIR on the R/V *Vickers* and the pyrgeometers on the NOAA P-3. The clear-sky FTIR measurements during daytime are identified by visual inspection of the sky above the detector. Contamination by downwelling flux from subvisible cirrus is less than the instrumental uncertainty in the measurements [*Lubin et al.*, 1995]. The resulting time series of $F_a(0)$ varies slowly with time along the ship track [*Lubin et al.*, 1995]. The values of $F_a(0)$ used to calculate $C_f(0)$ are linearly interpolated in time from the two nearest clear-sky observations. The clear-sky observations from the NOAA P-3 have been selected by comparing the measured net shortwave flux $S(0)$ with an estimate of the range of clear-sky flux $S_a(0)$ [*Li and Leighton*, 1993]. The data where $S(0)$ is within the range predicted for $S_a(0)$ are identified as clear-sky points (W.D. Collins et al., manuscript in preparation, 1995). The measurements of $F_a(0)$ have been parameterized in terms of the sea-surface and air temperatures by

$$F_a(T_s, T_a) = \varepsilon\sigma T_s^4 - \varepsilon_a\sigma T_a^4, \tag{11}$$

where $\varepsilon = 0.97$ and $\varepsilon_a = 0.852$ are the oceanic and atmospheric emissivities, respectively. The air temperature T_a is measured at the altitude of the P-3. The atmospheric emissivity is slightly smaller than the ε_a determined with the empirical formula by *Anderson* [1952]. The mean difference between $F_a(0)$ and $F_a(T_s, T_a)$ is 0.2 W m^{-2}, with a 6.4 W m^{-2} rms error. A histogram of the difference is shown in Figure 2.

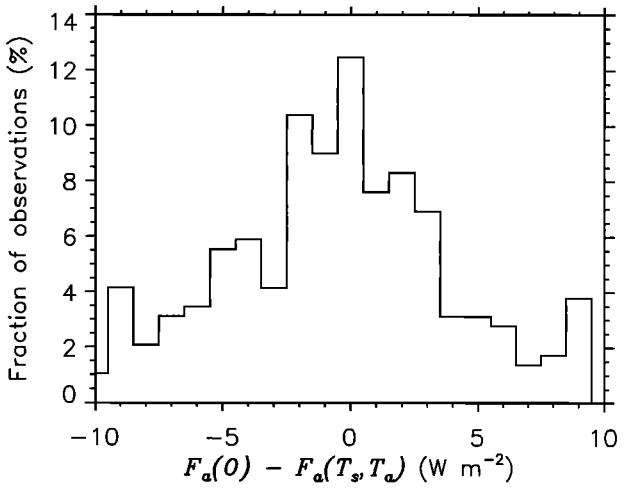

Figure 2. Difference between clear-sky net longwave flux $F_a(0)$ measured by the NOAA P-3 within 33 m of the ocean surface and the flux $F_a(T_s, T_a)$ calculated from (11). Ordinate axis is the percentage of flux differences within each 1 W m^{-2} bin on the abscissa.

2.3. Estimation of Fluxes for Cloudy Conditions

The cloud forcing is defined in terms of the daily mean shortwave and longwave fluxes. Since the longwave fluxes are not directly affected by the incident solar flux, the daily mean values of $F(0)$ and F(Trop) are unweighted averages of the longwave measurements. However, the shortwave fluxes are proportional to the insolation $S_0\cos(\theta)$, and daily averages of $S(0)$ and S(Trop) will differ from their true values if measurements are unavailable for certain Sun angles or if the time rate of change of θ is affected by the motion of the measurement platforms. The observations from the ER-2 and P-3 were made during daylight hours only, and the data sets do not include measurements at dawn and dusk when $\theta \cong 90°$. The largest zenith angles sampled by the ER-2 on individual flights range from 33° to 78°, and the largest zenith angles for P-3 low-altitude flights range from 20° to 52°. In addition, the variation of Sun angle with time measured from a moving platform is different from the motion of the Sun at a fixed position. The Sun angle changes more rapidly for an observer traveling eastward and more slowly for an observer traveling westward than for a stationary observer. Since the aircraft change direction several times during each flight, the solar zenith angles during the westbound segments have greater weight in time-averaged solar fluxes than the angles for eastbound segments.

In order to minimize the effects of incomplete diurnal sampling and motion of the instruments we have computed the daily mean shortwave fluxes using

$$\bar{S} = \frac{\langle S \rangle}{\langle S_0 \cos(\theta) \rangle} \langle \overline{S_0 \cos(\theta)} \rangle. \tag{12}$$

The angle brackets denote a time average over all the observations, and the horizontal bar denotes a time average from dawn to dusk at a fixed location. The first factor on the right-hand side is the ratio of the net shortwave radiation to the incident radiation for the measurement period. The second factor is the average of the diurnal mean incident solar flux for each point along the path of the platform. For the R/V *Vickers*, which is almost stationary, the effects of these corrections are small compared to the variations in the daily mean fluxes. Therefore the estimates of the daily surface insolation from equation (12) and an unweighted average of the measured fluxes should be virtually identical. During March 7 to March 22, 1993, $\langle S^{\downarrow}(0) \rangle$ ranges from 191 to 318 W m^{-2}. The estimates of insolation from $\langle S^{\downarrow}(0) \rangle$ and $\overline{S^{\downarrow}(0)}$ differ by less than

5 W m^{-2} during this period. This test confirms that (12) reduces to a simple time average for a stationary platform with complete diurnal sampling.

However, when the diurnal sampling is incomplete, $\overline{S}$ is a much better estimate of the daily mean flux than an unweighted average of the observations denoted by $\langle S \rangle$. Figure 3 shows the two estimates of the net surface insolation under clear-sky conditions as a function of the maximum solar zenith angle included in the averages. The insolation is calculated for the location 2°S, 180°E on March 15, 1993. For each point on the two curves, the flux is integrated from $\theta = 0$ (overhead sun) to the value of θ on the abscissa. The unweighted estimate $\langle S \rangle$ has a strong dependence on the range of solar zenith angle included in the averages. The weighted average given by (12) varies by less than 4%, or 12 W m^{-2}, over the range of θ. Since the weighted average is much less sensitive to the sampling of the diurnal cycle, we use (12) to calculate the clear-sky and average fluxes from all the shortwave measurements.

The upwelling and downwelling solar fluxes necessary to calculate $S(0)$ and $C_s(0)$ were measured on the NOAA P-3, but the upwelling flux was not measured on the R/V *Vickers*. By definition the upwelling flux is related to the downwelling flux by $S^+(0) = \alpha(0)S^-(0)$, where $\alpha(0)$ is the albedo of the ocean surface. The ocean albedo depends upon the relative amounts of direct and diffuse downwelling solar radiation under clear and cloudy conditions. This dependence may be formulated in terms of the atmospheric transmission [*Payne*, 1972]

$$t = \frac{S^-(0)}{S_0 \cos(\theta)}. \quad (13)$$

Under clear-sky conditions the atmosphere transmits approximately 80% of the incident radiation to the surface and absorbs the remaining 20%. Under overcast conditions with optically thick clouds the transmission can reach very low values. The ocean albedo $\alpha_{dir}(0,\theta)$ for mostly direct radiation under clear-sky conditions has been calculated by using the method of *Li and Garand* [1994] from the TOA albedo (equation 10), solar angle θ, and precipitable water p. The dependence of $\alpha_{dir}(0,\theta)$ on solar angle is shown in Figure 4. The ocean albedo estimated from the ratio of $S^+(0)$ and $S^-(0)$ measured close to the ocean surface from the NOAA P-3 is plotted for comparison. The measured and calculated albedos differ by less than 1% (absolute) for $\theta < 53°$.

The ocean surface albedo for diffuse radiation is estimated from the P-3 measurements. The measured albedo is shown as a function of atmospheric transmission t in Figure 5. The ocean albedo for diffuse radiation is set to the limiting value $\alpha_{diff}(0) = 0.057$ for $t \approx 0$. For combinations of direct and diffuse radiation the albedo is intermediate between the direct and diffuse albedos, and it is linear in t to lowest order [*Payne*, 1972]. The linear relationship is demonstrated with the P-3 measurements shown in Figure 5. Thus the ocean albedo may be approximated by

$$\alpha(0) = \alpha_{diff}(0) + \left[\frac{\min(t, t_a)}{t_a}\right][\alpha_{dir}(0,\theta) - \alpha_{diff}(0)], \quad (14)$$

where t_a is the clear-sky atmospheric transmission. The clear transmission is computed from the net surface flux $S_a(0)$ [*Li and Leighton*, 1993] and the albedo for direct radiation $\alpha_{dir}(0,\theta)$ [*Li and Garand*, 1994] by $t_a = S_a(0) / [1 - \alpha_{dir}(0,\theta)]$. Since $\alpha(0)$ is close to a local maximum or minimum when $t \approx t_a$, the transmission t is constrained to be less than t_a. The measurements of $S^-(0)$ and equation (14) for $\alpha(0)$ are used to calculate the net solar flux.

2.4 Satellite Classification of Cloud Type

The type of cloud measured by the surface and tropospheric platforms is classified by an effective cloud top, or brightness, temperature. In regions of deep tropical convection the cloud forcing is closely correlated with the presence of high, optically thick clouds [*Kiehl*, 1994]. On an annual basis, most of the variance in albedo and outgoing longwave radiation (OLR) is correlated with high cloud cover for these regions [*Ockert-Bell and Hartmann*, 1992]. Because the convective clouds are much colder than the ocean surface, the area mean cloud top temperature is determined primarily by the amount of high cloud cover. These high clouds may be several kilometers thick in the tropics. The relation of

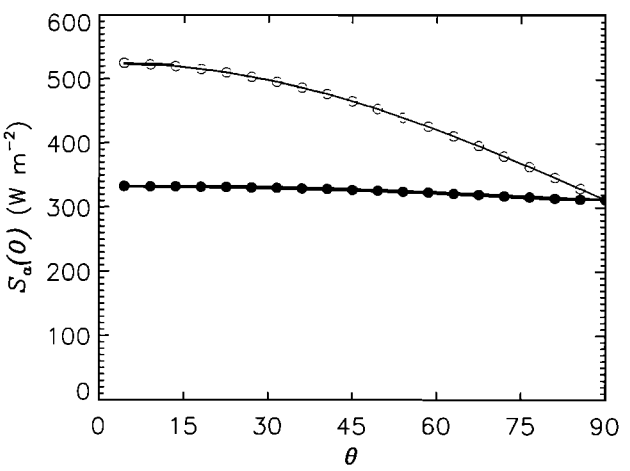

Figure 3. Estimates of daily mean clear-sky surface shortwave flux as a function of the range of solar zenith angles included in the averages. Solid symbols indicate $\overline{S_a(0)}$ calculated from (12). Open symbols show $f\langle S_a(0)\rangle$, where f is the fraction of daylight hours. $S_a(0)$ is calculated from the *Li and Leighton* [1993] parameterization for the net clear-sky solar flux with a TOA albedo given by (10) and with 4.5 cm of precipitable water. The calculation is for a fixed point at 2°S, 180°E on March 15, 1993.

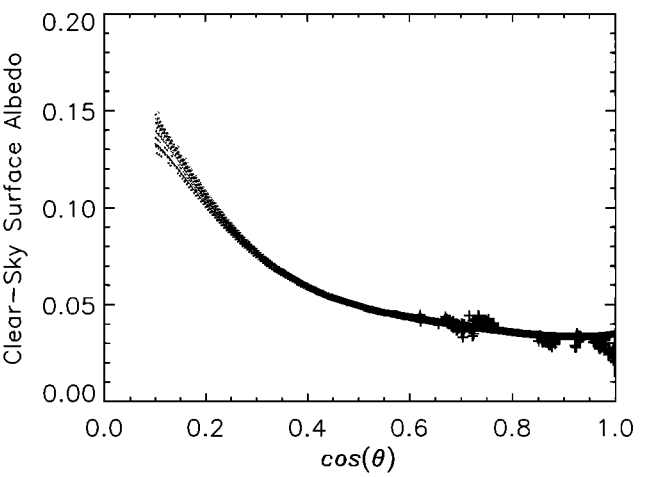

Figure 4. Ocean albedo $\alpha_{dir}(0,\theta)$ for clear-sky radiation as a function of solar zenith angle. Solid points show $\alpha_{dir}(0,\theta)$ calculated for the R/V *Vickers* from March 7 to March 22, 1993, using the method of *Li and Garand* [1994]. Precipitable water is interpolated in time between radiosonde profiles. Crosses indicate $\alpha_{dir}(0, \theta)$ estimated from the ratio of upwelling to downwelling shortwave flux within 33 m of ocean surface from the NOAA P-3.

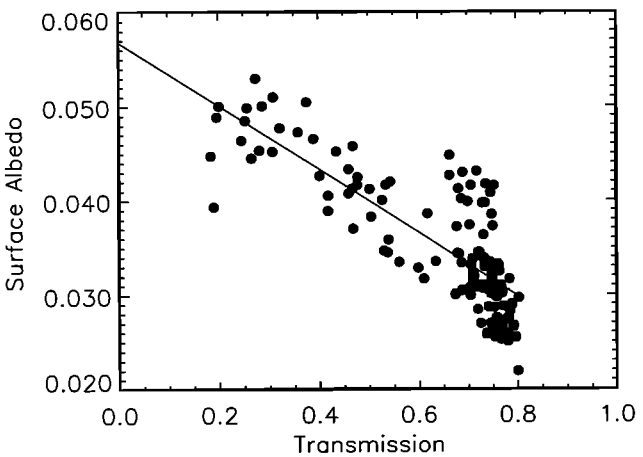

Figure 5. Ocean albedo $\alpha(0)$ as a function of atmospheric transmission t. Solid symbols indicate $\alpha(0)$ estimated from the ratio of upwelling to downwelling shortwave flux measured by the NOAA P-3. The transmission is given by (13). Fluxes are averaged over 3 min, and points with $S^+(0)$ less than 10 W m^{-2} have been omitted. The solid line shows least squares linear regression of t and $\alpha(0)$. The diffuse albedo $\alpha_{diff}(0) = 0.057$ is the value of $\alpha(0)$ at $t = 0$.

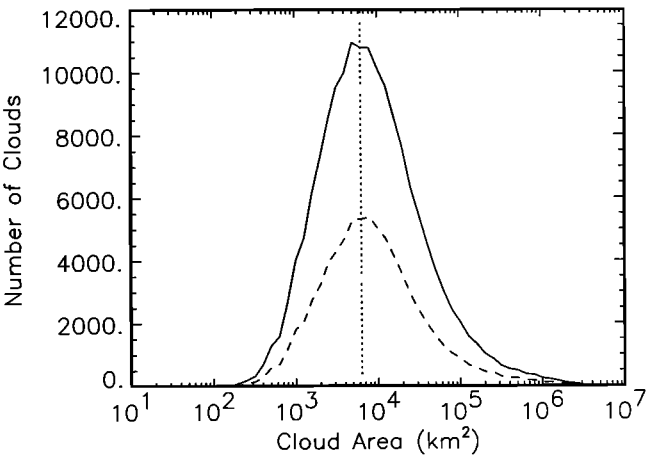

Figure 6. Number of clouds with min $(T_c) < 233$ K as a function of cloud surface area A_c. The cloud area bins are logarithmic, and the width of the bins is log $(A_c) = 0.1$. Clouds detected in GMS satellite images in the region 20°N to 20°S, 120°E to 160°W during March 7 to April 5, 1993, are included. The statistics are based upon 160,876 clouds, with 74,988 clouds identified during daylight conditions. The solid line shows distribution of A_c for all clouds; the dashed line, distribution of A_c for clouds during daytime; and the dotted line, median cloud area $A_c = 6310$ km^2.

cloud forcing and cloud temperature to cloud cover suggests that the cloud forcing and temperature should be closely correlated for tropical oceanic regions. This correlation is demonstrated with the CEPEX observations.

Infrared brightness temperatures (IRBT) have been measured with the Japanese Geostationary Meteorological Satellite (GMS-4) [*Murayama*, 1989]. The satellite includes an imaging spectral radiometer that measures radiances in the midinfrared window between 10 and 12 μm [*Rossow et al.*, 1992]. The radiances are converted to IRBT for an equivalent blackbody source. For an optically thick cloud in the middle to upper troposphere the IRBT is very close to the cloud top temperature. For an optically thin cloud the IRBT is higher than the cloud temperature because the satellite radiance includes emission from the warm ocean surface. Infrared images of the CEPEX domain with 5 km pixel resolution were collected at 60 min intervals during the experiment. The IRBT for the clouds measured by each platform have been extracted from the images by using the satellite observations closest in space and time. The IRBT are averaged over a square region centered on each platform to give an area mean value T_c.

The size of the averaging region has been determined from the characteristic dimensions of cold clouds. The clouds in each infrared image have been identified with a cloud classification algorithm (Boer, E. R., and V. Ramanathan, Satellite based approach for modeling clouds in GCMs, submitted to J. Geophys. Res., 1995). The procedure classifies each connected region with IRBTs less than 285 K into one of eight different cloud types based upon the minimum IRBT within the region. The analysis does not consider the previous history of the cloud field, so that an individual cloud may be counted several times during its evolution. The distribution of surface area for clouds with minimum IRBT below 233 K and maximum IRBT less than 285 K is shown in Figure 6. The lower threshold temperature, which is the homogeneous nucleation temperature for ice particles [*Heymsfield and Sabin*, 1989], insures that the clouds have significant ice content and extend into the upper troposphere. The median area for the cloud frequency distribution is $A_c = 6310$ km^2. The area corresponding to the peak in the frequency distribution is also approximately 6000 km^2. The size of the averaging region is set to 6000 km^2 in the analysis that follows. This surface area corresponds to a class I system in the TOGA COARE classification of convection [*Webster and Lukas*, 1992].

Variations in the area-averaged IRBT are related to several factors, including changes in cloud cover, cloud optical thickness, and cloud top temperature. The area-averaged IRBT is preferable to derived quantities such as cloud cover as an index of cloud effect for several reasons: IRBT is measured directly, estimates of cloud cover from satellite imagery derived with different algorithms do not converge at the resolution of the GMS radiometers [*Wielicki and Parker*, 1992], and the cloud amounts over oceans obtained from *in situ* and remote sensing data can differ significantly [*Haskins et al.*, 1995]. In this application the principal issue is the detection of sub-pixel-scale trade cumulus. The trade cumulus can have a substantial effect on the surface insolation but may be difficult to detect in satellite imagery because the clouds are smaller than the spatial resolution of the image pixels. By using area-averaged IRBT the broken cumulus are mapped to values of T_c close to the values for clear regions, approximately 290 K.

3. Cloud Forcing From *In Situ* Measurements

3.1. Tropopause Cloud Forcing

Figures 7a and 7b show the daily mean C_l(Trop) and C_s(Trop) for each flight of the ER-2 as a function of the daily mean brightness temperature $\overline{T_c}$. The numerical values of C_l, C_s and the estimates of the clear-sky fluxes are given in Table 1. The maximum cloud forcing was measured during a dedicated microphysics mission on April 4, 1993, when the ER-2 flew above a region of active convection and extended cirrus anvil clouds. The daily mean cloud forcing for this convective system is C_l(Trop) = 138 W m^{-2} and C_s(Trop) = −136 W m^{-2}. The magnitudes of the shortwave and

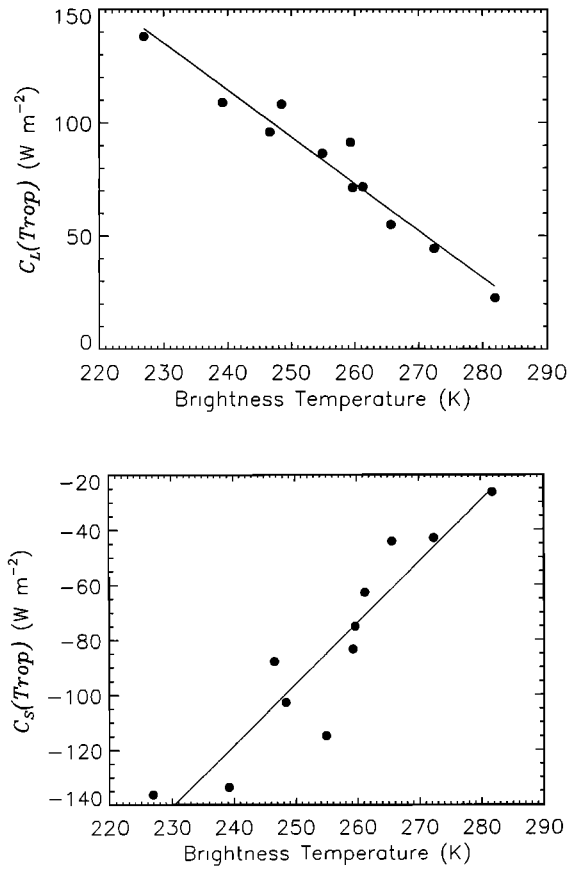

Figure 7. (a) C_l(Trop) as a function of $\overline{T_c}$ for each flight of the NASA ER-2. Each point represents the average cloud forcing for a single flight (Table 1). $\overline{T_c}$ is the average over each flight of the instantaneous area average IRBT in a 6000 km^2 domain around the aircraft. The solid line shows the least squares regression fit given by (15). (b) C_s(Trop) as a function of $\overline{T_c}$. The solid line shows the least squares regression fit (16).

longwave cloud forcing increase monotonically with decreasing $\overline{T_c}$. Regression of the cloud forcing against $\overline{T_c}$ by linear least squares explains 86% of the variance in C_s(Trop) and 95% of the variance in C_l(Trop). The relation of the cloud forcing to $\overline{T_c}$ obtained from the regression is

$$C_l(\text{Trop}) = 2.1\ (290 - \overline{T_c}) + 11, \quad (15)$$

$$C_s(\text{Trop}) = -2.2\ (290 - \overline{T_c}) - 4. \quad (16)$$

The factors that reduce the IRBT, including increased cloud infrared emissivity, cloud cover, and temperature gradients between the surface and cloud top, also reduce the OLR and increase C_l(Trop). Changes in cloud cover and cloud emissivity also change the albedo. Since the cloud albedo is generally larger than the clear-sky albedo, an increase in cloud cover with all other cloud properties held constant decreases T_c and increases the magnitude of C_s(Trop). The cloud emissivity and cloud albedo are related by the optical depths τ_{ext} and τ_{abs} for visible extinction and infrared absorption respectively. The ratio τ_{ext}/τ_{abs} is approximately 2.0 for large ice and water droplets [*van de Hulst*, 1981], and it is positive for smaller particles. Therefore increased infrared absorption in clouds is accompanied by more extinction of the incident solar radiation. The link between extinction and absorption provides a qualitative explanation for the correlation between C_s(Trop) and $\overline{T_c}$.

The shortwave and longwave cloud forcing are approximately equal in magnitude. Figure 8 shows the relation between the two cloud forcing terms for 10 flights. Least squares regression of the cloud forcing terms yields

$$C_s(\text{Trop}) = -1.04\ C_l(\text{Trop}) + 4.2. \quad (17)$$

The regression explains 87% of the covariance between C_l(Trop) and C_s(Trop). The sum of (15) and (16) gives the variation of the net cloud forcing C_{net}(Trop) with brightness temperature. The average of C_{net}(Trop) for the CEPEX observing period is less than 1 W m^{-2}. The net forcing is less than 2% of the average longwave and shortwave cloud forcing. The cancellation between C_l(Trop) and C_s(Trop) on monthly time scales has been previously observed in the ERBE satellite data [*Ramanathan et al.*, 1989; *Harrison et al.*, 1990]. The small value of C_{net}(Trop) for the research flight on April 4 is of particular interest, since most of the observations were collected for a single cloud system. The mission consisted of seven colinear overpasses above a line of convective cells and the attached anvil for 80% of the total flight time. The length of the overpasses was 195 km, which is less than the dimensions of the ERBE grid boxes at the latitude of this cloud system. The ER-2 was not permitted to fly close to or above convective turrets, and therefore the cloud forcing is determined

Table 1. Diurnally Averaged Shortwave, Longwave, and Net Cloud Forcing for Each ER-2 Flight

Date UTC	C_s(Trop), W m^{-2}	C_l(Trop), W m^{-2}	C_{net}(Trop), W m^{-2}	S_a^+(Trop), W m^{-2}	F_a(Trop), W m^{-2}	$\overline{T_c}$, K
March 11, 1993	-27.	23.	-4.	35.	267.	282.
March 15	-63.	72.	9.	34.	267.	261.
March 16	-103.	108.	5.	33.	264.	248.
March 17	-134.	109.	-25.	33.	264.	239.
March 23	-44.	55.	11.	33.	266.	266.
March 25	-83.	91.	8.	33.	266.	259.
March 28	-43.	44.	1.	33.	267.	272.
March 30	-75.	71.	-4.	33.	266.	260.
April 4	-136.	138.	2.	32.	266.	227
April 5, 1993	-88.	96.	8.	32.	265.	247.

C_s and C_l are calculated by using (1), (2), and (12). The mean shortwave and longwave clear-sky fluxes are estimated by using (8), (9), (10), and (12). The spectral bandwidth of F_a(Trop) is 4-40 μm.

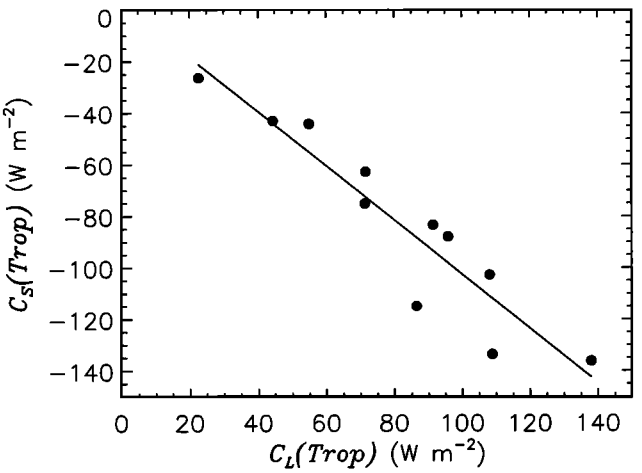

Figure 8. C_S(Trop) versus C_I(Trop) for each flight of the NASA ER-2. Each point represents a single flight (Table 1). The solid line shows the least squares linear regression given by (17).

primarily by the radiative effects of the anvil. This demonstrates that the cancellation of cloud forcing can occur for a single cloud system on timescales less than or equal to 1 day and spatial scales comparable to the dimensions of the system. The average of C_{net}(Trop) for 10 flights is less than 3% of S_a^+(Trop) and is less than 1% of F_a^+(Trop). The observations show that the heat budget of the surface-troposphere system is not appreciably changed by the presence of convective clouds.

3.2. Surface Cloud Forcing

The variation of the daily mean $C_S(0)$ with $\overline{T_c}$ is shown in Figure 9. The estimates of $C_S(0)$ and $\overline{T_c}$ from the R/V *Vickers* and the NOAA P-3 are listed in Table 2. The differences between the values of $C_S(0)$ from the two platforms on a given day occur because the ship and aircraft sampled different geographic regions. The differences between the values of $S_a(0)$ occur because most of the P-3 measurements at low altitude were made

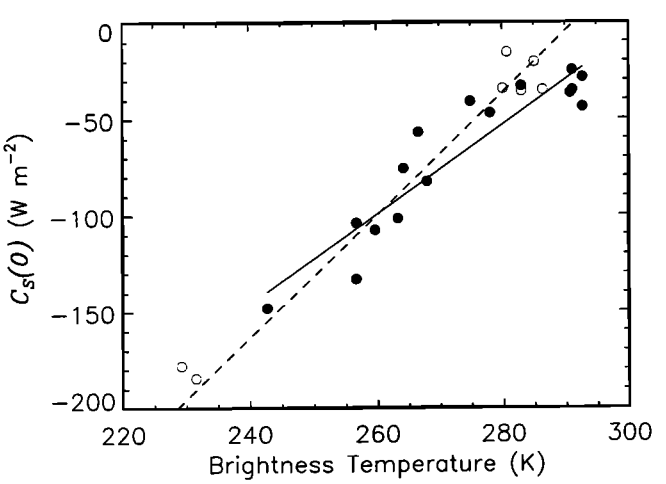

Figure 9. $C_S(0)$ as a function of $\overline{T_c}$. Solid symbols indicate daily mean cloud forcing from the R/V *Vickers* data (Table 2). Open symbols show daily mean cloud forcing from the NOAA P-3. The solid line shows least squares regression fit given by (18); and the dashed line, the least squares regression fit (19), excluding days with $\overline{T_c}$ greater than 290 K.

Table 2. Diurnally Averaged Shortwave Cloud Forcing for Each Day of R/V *Vickers* and NOAA P-3 Pyranometer Observations

Date UTC	$C_S(0)$, W m^{-2}	$S_a(0)$, W m^{-2}	$\overline{T_c}$, K	$\sigma(T_c)$, K
		R/V *Vickers*		
March 7, 1993	−83.	313.	268.	3.
March 8	−148.	313.	243.	5.
March 9	−104.	310.	257.	18.
March 10	−76.	311.	264.	8.
March 11	−44.	313.	293.	< 1.
March 12	−37.	316.	291.	1.
March 13	−29.	317.	293.	< 1.
March 14	−47.	319.	278.	12.
March 15	−33.	318.	283.	10.
March 16	−35.	316.	291.	< 1
March 17	−25.	316.	291.	1.
March 18	−133.	309.	257.	5.
March 19	−41.	311.	275.	12.
March 20	−102.	309.	263.	14.
March 21	−57.	310.	267.	16.
March 22, 1993	−108.	316.	260.	17.
		NOAA P-3		
March 14, 1993	−21.	329.	285.	6.
March 15	−16.	331.	281.	10.
March 16	−35.	333.	286.	4.
March 25	−36.	315.	283.	12.
March 26	−184.	323.	232.	8.
April 3	−178.	320.	229.	15.
April 4, 1993	−34.	321.	280.	21.

The fluxes are computed with the same equations as those used in Table 1. The averages exclude observations with $\theta > 85°$. The standard deviation of T_c during each day is given by $\sigma(T_c)$.

for nearly overhead sun (see Figure 3). The magnitude of $C_S(0)$ increases with decreasing $\overline{T_c}$, with a maximum forcing of $C_S(0)$ = −184 W m^{-2} for $\overline{T_c}$ equal to 232 K. Since $S_a(0)$ = 323 W m^{-2}, the clouds reduce the surface insolation to 139 W m^{-2}, 43% of the daily mean clear-sky value. The minimum cloud forcing in the R/V *Vickers* observations is $C_S(0)$ = −25 W m^{-2}, and the corresponding $\overline{T_c}$ is 291 K. Values of $\overline{T_c}$ greater than 290 K are close to the range of IRBT measured for cloudless conditions (W.D. Collins et al., unpublished manuscript, 1995). The average cloud forcing for the days when $\overline{T_c}$ is greater than 290 K is −34 W m^{-2}. The magnitude of the cloud forcing suggests that the atmosphere is convectively disturbed and cloudy despite the relatively high IRBT. The two types of clouds consistent with the value of $\overline{T_c}$ are optically thick clouds within the boundary layer and optically thin middle and upper level clouds [*Wielicki and Parker*, 1992]. Visual inspection of the cloud field from the ship confirms that the predominant cloud types on the days when $\overline{T_c}$ is greater than 290 K are low-altitude scattered cumulus and/or thin cirrus.

The relation of $C_S(0)$ to $\overline{T_c}$ from least squares regression of the R/V *Vickers* observations is

$$C_S(0) = -2.3\,(290 - \overline{T_c}) - 30. \qquad (18)$$

If the days when $\overline{T_c}$ is greater than or equal to 290 K are omitted from the regression, the relation is

$$C_S(0) = -3.2\,(290 - T_c) - 5. \qquad (19)$$

This equation explains 89% of the variance in $C_S(0)$ for $\overline{T_c}$ less than 290 K.

When $C_s(0)$ and $C_s(\text{Trop})$ are determined simultaneously, the difference between $C_s(0)$ and $C_s(\text{Trop})$ gives the divergence of solar flux into the cloudy atmosphere. Analysis of aircraft measurements from CEPEX [*Pilewskie and Valero*, 1995] and surface and satellite measurements [*Cess et al.*, 1995; *Ramanathan et al.*, 1995] show that $C_s(0)$ can exceed $C_s(\text{Trop})$ by 50% in tropical regions. These findings differ from calculations with radiative transfer models, which indicate that the absorption of shortwave radiation by clouds should be a small fraction of $C_s(\text{Trop})$ [*Stephens and Tsay*, 1991].

Since the observations from the ER-2 and R/V *Vickers* were made at different times and locations, the tropospheric and surface cloud forcing were determined for different cloud systems. Estimates of cloud absorption are very sensitive to the spatial and temporal coincidence between the radiative measurements above and below the cloud layer [*Fouquart et al.*, 1990]. When the measurements are not coincident, the effects of inhomogeneities and dynamical evolution of the cloud layer can yield large uncertainties in the amount of shortwave absorption. For this reason the difference between $C_s(\text{Trop})$ given by (16) and $C_s(0)$ given by (18) or (19) may not be a reliable measure of $C_s(\text{A})$, the shortwave absorption by the cloudy atmosphere. We use these equations instead to derive a range of $C_s(\text{A})$ for a given value of $\overline{T_c}$.

The variation of the daily mean longwave cloud forcing with brightness temperature is shown in Figure 10. The estimates of $C_l(0)$ are from the FTIR on the R/V *Vickers* and the pyrgeometers on the P-3. The values of daily mean cloud forcing and brightness temperature for the FTIR instrument are given in Table 3. The relation of $C_l(0)$ to $\overline{T_c}$ is divided into two distinct clusters of points. In the first cluster, $\overline{T_c}$ exceeds 280 K, and the cloud forcing ranges between 0 and 50 W m^{-2}. The cloud forcing is nearly uncorrelated with the emission temperature measured from satellite. In the second cluster the cloud forcing increases gradually with decreasing IRBT. Radiative model calculations show that the first population corresponds to clouds near the ocean surface or thin cirrus, and the second population corresponds to deep convective clouds [*Harshvardhan et al.*, 1990]. Optically thick clouds near the surface have an infrared emissivity $\varepsilon \cong 1$, while the effective emissivity of the atmosphere is $\varepsilon_a \cong 0.852$ (equation 11). The difference in longwave emission from a cloud and the atmosphere

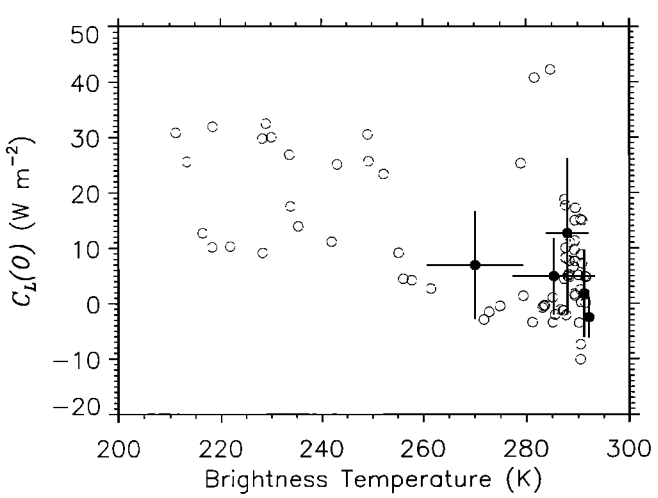

Figure 10. $C_l(0)$ as a function of $\overline{T_c}$. Solid symbols indicate daily mean cloud forcing from the R/V *Vickers* FTIR data (Table 3). Horizontal error bars indicate the rms standard deviation of the IRBT, and vertical error bars indicate the rms standard deviation of $C_l(0)$. Open symbols show cloud forcing averaged over 180 s of flight time from the P-3 pyrgeometer measurements.

Table 3. Longwave Cloud Forcing for Each Day of R/V *Vickers* FTIR Observations

Date UTC	$C_l(0)$, W m^{-2}	$\sigma(C_l)$, W m^{-2}	$\overline{T_c}$, K	$\sigma(T_c)$, K
March 7, 1993	10.	10.	266.	7.
March 9	18.	11.	268.	7.
March 10	10.	8.	263.	10.
March 11	−2.	2.	293.	1.
March 12	13.	13.	288.	4.
March 13	−2.	4.	292.	< 1.
March 14	7.	10.	270.	9.
March 15	5.	7.	285.	8.
March 16	2.	8.	291.	< 1.
March 17	6.	7.	290.	2.
March 19	5.	10.	275.	6.
March 20	10.	12.	267.	7.
March 21, 1993	1.	5.	271.	7.

The averages include measurements between 1200 UTC (approximate local midnight) on the starting date and 1200 UTC on the following date. Here $\sigma(T_c)$ is the root-mean-square standard deviation of the temperature within a 6000 km^2 domain centered on the R/V *Vickers*, and $\sigma(C_l)$ is the standard deviation of the instantaneous values of $C_l(0)$ averaged to obtain the daily mean.

can produce a substantial cloud forcing when the cloud is close to the surface. The mean $C_l(0)$ for the first cluster with $\overline{T_c}$ greater than 280 K is between 4 and 6 W m^{-2}.

The relation of $C_l(0)$ and $\overline{T_c}$ for the second cluster obtained from least squares regression is

$$C_l(0) = 0.37\,(290 - \overline{T_c}) - 2. \qquad (20)$$

The correlation between the cloud forcing and IRBT is $r = -0.57$ and is statistically significant. Although equations (15) and (20) are derived from observations of different cloud systems, the ratio of $C_l(0)$ to $C_l(\text{Trop})$ is consistent with coincident observations at the surface and top of the atmosphere (W.D. Collins et al., manuscript in preparation, 1995). The surface cloud forcing is generally less than 20% of the TOA cloud forcing for the coldest clouds. The difference between $C_l(0)$ and $C_l(\text{Trop})$ indicates that most of the longwave emission from colder clouds is absorbed in the troposphere.

The sum of (19) and (20) gives the variation of $C_{net}(0)$ with IRBT as

$$C_{net}(0) = -2.8\,(290 - \overline{T_c}) - 7. \qquad (21)$$

This relation is applicable when $\overline{T_c}$ is less than 280 K. The CEPEX observations show that the net effect of cold clouds is to cool the ocean surface. For example, when the daily mean IRBT over a particular region is 240 K, the net surface cloud forcing is approximately −147 W m^{-2}. When the clouds are warmer than 280 K, the average of the R/V *Vickers* observations gives $C_{net}(0) = -30$ W m^{-2} (Tables 2 and 3). This cloud forcing is associated with low-altitude cumulus clouds. The difference between $C_{net}(\text{Trop})$ and $C_{net}(0)$ is the cloud forcing on the atmosphere. From (15), (16), and (21), $C_{net}(A)$ is given by

$$C_{net}(A) = 2.7\,(290 - \overline{T_c}) + 15. \qquad (22)$$

Because the magnitude of $C_{net}(\text{Trop})$ is much less than $C_{net}(0)$, $C_{net}(\text{A})$ is nearly equal and opposite to $C_{net}(0)$. The vertical distribution of cloud forcing in the CEPEX region has a dipole form,

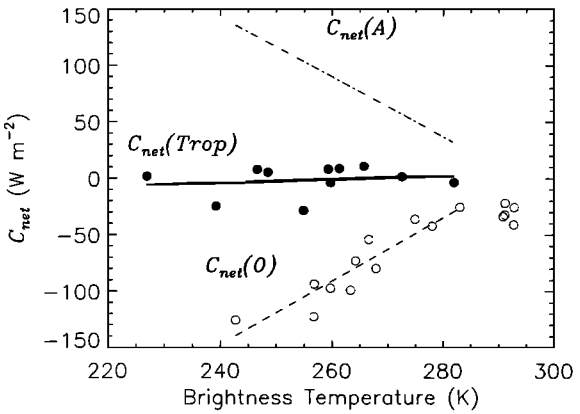

Figure 11. Daily mean C_{net}(Trop) and C_{net}(0) as a function of $\overline{T_c}$. The solid line shows linear regression of C_{net}(Trop) (solid symbols) in terms of $\overline{T_c}$ from (15) and (16). The dashed line shows linear regression of C_{net}(0) (open symbols) in terms of $\overline{T_c}$ given by (21). The dash-dotted line shows the estimate of C_{net}(A) from (22).

with radiative cooling of the ocean surface and radiative heating of the overlaying atmosphere. The variation of the net cloud forcing on the surface, troposphere, and surface-tropospheric column with IRBT is shown in Figure 11. The magnitude of the dipole radiative effect increases rapidly as the brightness temperature decreases. This structure is a consequence of the small tropospheric cloud forcing and the longwave opacity of the atmosphere [*Ramanathan et al.*, 1989]. The estimate of $C_{net}(A)$ is uncertain, since the measurements at the surface and tropopause are not coincident. However, on timescales of a month or longer, $C_{net}(A)$ will probably have the general form shown in Figure 11, because the cancellation of C_{net}(Trop) is a persistent property of tropical clouds [*Harrison et al.*, 1990].

4. Regional Variation of Cloud Forcing and Convection

The CEPEX observations indicate that variations in the surface cloud forcing are determined primarily by variations in convective and cirrus cloud cover. The radiative effect of high clouds

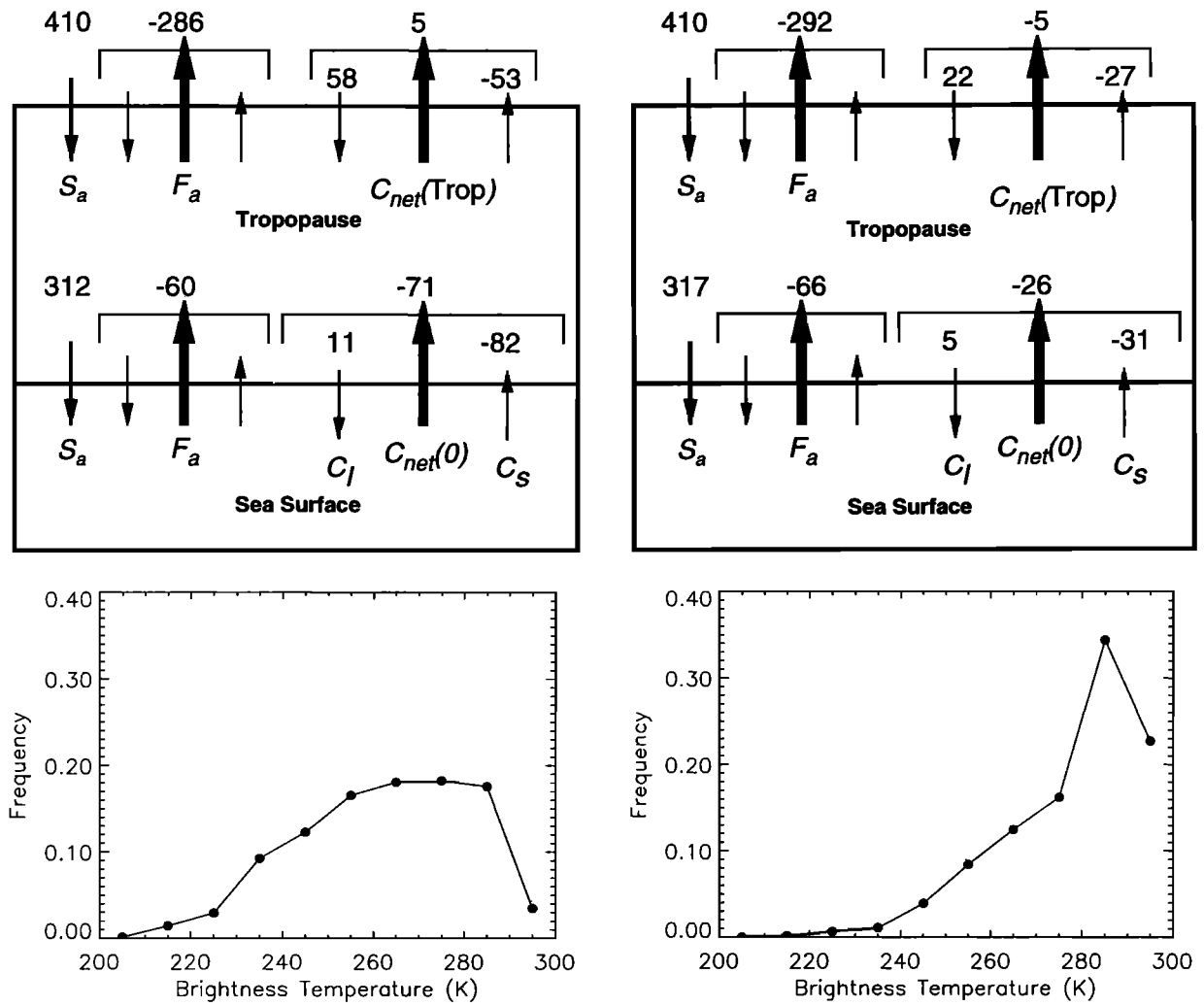

Figure 12. Clear-sky and cloud radiative fluxes in the CEPEX observing domain averaged over the CEPEX observing period. The arrows show the direction of the vectorial flux, and the sign of the flux is negative if the flux is directed away from the ocean surface. (a) Fluxes in the western domain between 3°S and 3°N, 160°E to 180°E. (b) Distribution of daily average $\overline{T_c}$ in the western domain between March 7 and April 7, 1993. (c) Fluxes in the eastern domain between 3°S and 3°N, 180°W to 160°W. (d) Distribution of $\overline{T_c}$ in the eastern domain between March 7 and April 7, 1993.

is evident in the zonal gradients of the radiative fluxes measured during CEPEX. The average clear-sky fluxes and cloud forcing at the surface and tropopause west and east of the dateline are shown in Figures 12a and 12c, respectively. The terms are averages of the daily mean fluxes calculated by using observations between 3°S and 3°N from 160°E to 180°E (hereafter the western domain) and 180°W to 160°W (hereafter the eastern domain). The net clear-sky longwave terms F_a have been calculated from atmospheric soundings of temperature and humidity [*Weaver et al.*, 1994] and validated with shipboard pyrgeometer measurements. The clear-sky shortwave and longwave terms S_a and F_a change by less than 7 W m^{-2} between the eastern and western domains. The largest change is the increase in the magnitude of $C_s(0)$ by 51 W m^{-2}. Since the corresponding change in $C_f(0)$ is 6 W m^{-2}, the net cloud forcing at the surface decreases from –26 W m^{-2} to –71 W m^{-2} from east to west. The vertical divergence of cloud radiative forcing should be interpreted with caution because the surface and airborne measurements are not coincident.

In the absence of a detailed characterization of the cloud morphology we have used the satellite brightness temperature to characterize the cloud populations observed from the surface and airborne platforms. While this parameter is insensitive to the specific geometry of the clouds, it does provide an index of convective activity. The distributions of IRBT in the two domains are shown in Figures 12b and 12d for March 7 to April 7, 1993. In the east the most frequent temperature and the median temperature are approximately 285 K. In the west the median brightness temperature is 264 K, and the distribution has a broad peak between 260 and 280 K. The mean and median brightness temperatures coincident with the ship and aircraft observations used to calculate the terms in Figure 12 are given in Table 4. The statistics indicate that the frequency of convection observed by the surface and airborne instruments is similar in both eastern and western domains. The satellite observations show that the reduction in surface insolation is associated with increased frequency of cold clouds.

The number of clouds and the fractional cloud cover with a minimum IRBT below 240 K in the tropical and subtropical Pacific are plotted as a function of sea surface temperature (SST) in Figure 13. Both the number and the fractional cloud coverage increase rapidly with T_s starting at 298 K. The maximum number of clouds is observed between 302 and 302.5 K, and the number declines rapidly at higher temperatures. The reduction in cloud number is related to the reduction in the fraction of the ocean surface warmer than 302.5 K. Despite the declining number of clouds the cloud cover exceeds 50% at the highest surface temperatures. It is important to note that the observations do not indicate a local relationship between SST and convective frequency.

Table 4. Mean and Median Values of Area-Averaged Satellite IRBT Coincident with Ship and Aircraft Measurements Near the Equator

	Western Domain		Eastern Domain	
	Mean T_c, K	Median T_c, K	Mean T_c, K	Median T_c, K
NASA ER-2	283±11	291	266±26	272
R/V *Vickers*	287±6	291	264±21	269

The IRBT is averaged over a 6000 km^2 area centered on the measurement platforms. The western domain is 3°S to 3°N from 160°E to 180°E, and the eastern domain is 3°S to 3°N from 180°W to 160°W. The statistics are calculated for all the observations by the ER-2 and R/V *Vickers* in the eastern and western domains during CEPEX.

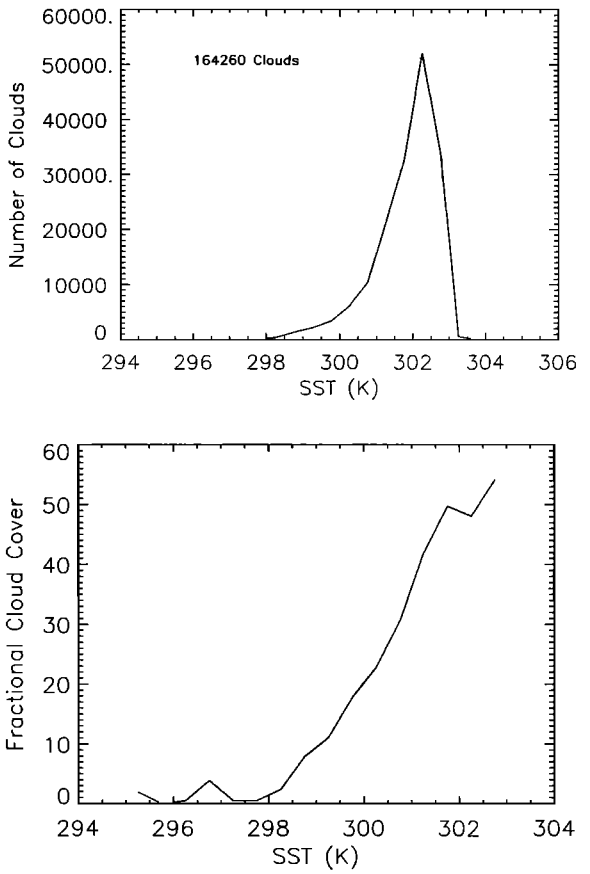

Figure 13. Distribution of clouds with min (T_c) < 240 K as a function of SST. Clouds detected in GMS satellite images for the region 20°N to 20°S, 160°E to 160°W during March 7 to April 5, 1993, are included. The statistics are based upon 164,260 clouds. (a) Number of clouds versus T_s. (b) Fractional cloud cover versus T_s.

The onset of convection is governed by both local and nonlocal mechanisms [*Hartmann and Michelsen*, 1993; *Lau et al.*, 1994; *Ramanathan et al.*, 1994]. Although the relative importance of the various mechanisms is still unclear, the frequency of convection increases with ocean temperatures up to 302.5 K. The smooth increase in convective activity with SST starting at approximately 300 K during CEPEX is qualitatively similar to the trends observed in decadal-length satellite data sets [*Waliser and Graham*, 1993; *Zhang*, 1993].

The change in the cloud cover with T_s is accompanied by changes in the probability distribution $f(\overline{T}_c, T_s)$ of IRBT. The integrated distribution

$$p(T_c, \overline{T}_s) = \int_0^{\overline{T}_c} f(T', T_s)\, dT' \tag{23}$$

of IRBT with T_s is shown in Figure 14 for the CEPEX domain. The distribution is calculated from the daily mean IRBTs averaged on a 6000 km^2 grid. The contours indicate the fraction of brightness temperatures below the contour ordinate at a given SST; for example, approximately 50% (0.5) of the IRBTs in the CEPEX domain are less than 260 K when the SST is 303 K. The median IRBT exceeds 290 K when T_s is below 300 K. Therefore during CEPEX most of the cloud cover for oceans colder than 300 K is composed of low-altitude clouds or thin cirrus. The median IRBT decreases by approximately 10 K for each 1 K increase in T_s. For SST above 303 K the median IRBT is below 260 K.

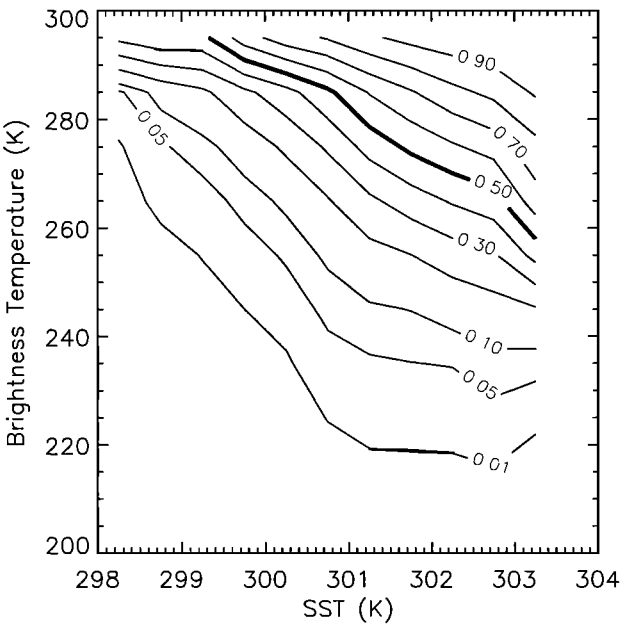

Figure 14. Integrated probability $p(\overline{T}_c, T_s)$ of brightness temperatures (equation 23) as a function of T_s. The probability is calculated from the same data as were used in Figure 13. Brightness temperatures are averaged over 6000 km^2. Contours show the frequency of IRBT below the corresponding ordinate at a given SST. The contour interval is 0.1 except for the contours labeled 0.01 and 0.05. The contour for the median IRBT is denoted with a thick line.

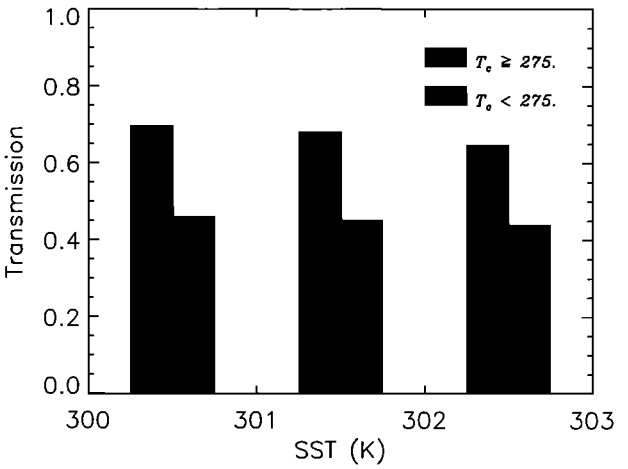

Figure 15. Atmospheric transmission calculated from the R/V *Vickers* pyranometer measurements (13) as a function of SST. The gray and black bars are the transmission for clouds with $\overline{T}_c$ greater than and less than the median value of 275 K, respectively. The data cover the same time interval as Table 2.

The distribution of IRBT with SST and the correlation of IRBT and surface cloud forcing (Figure 11) imply that the reduction of surface insolation by clouds increases with ocean temperature. The relation of the surface cloud forcing to SST can be estimated by integrating the cloud forcing over IRBT weighted by the distribution of IRBT. The surface shortwave cloud forcing may be written in the form

$$C_s(T_s) = \int C_s(\overline{T}_c)\ f(\overline{T}_c, T_s)\, d\overline{T}_c. \tag{24}$$

The relation of $C_s(0)$ to $\overline{T}_c$ is given by (18) and (19), and the probability of T_c at a fixed SST is denoted by $f(\overline{T}_c, T_s)$. A similar relation applies to the surface longwave cloud forcing. This method for calculating the change in surface cloud forcing with T_s is valid only if the statistical correlation between cloud forcing and IRBT does not depend on T_s. The shortwave cloud forcing is linearly related to the atmospheric transmission (13) through the average downwelling solar flux (12). The transmission estimated from the R/V *Vickers* data under cloudy conditions is shown as a function of SST in Figure 15. The transmission is plotted separately for clouds with T_c above and below 275 K, the median IRBT for the clouds observed from the R/V *Vickers*. The transmission for the two ranges of IRBT varies by less than 5% over a 3 K range in SST. This indicates that the optical properties of the clouds observed from the surface platforms do not depend explicitly on SST.

The variation of $C_l(0)$ and $C_s(0)$ with SST in the central Pacific estimated from (24) is shown in Figure 16. For regions with $\overline{T}_c$ below 280 K, (19) and (20) are used to estimate $C_s(0)$ and $C_l(0)$. For regions with $\overline{T}_c$ greater than 280 K, $C_s(0)$ and $C_l(0)$ are held fixed at the observed values of –30 W m^{-2} and 4 W m^{-2}, respectively. The 2σ confidence intervals determined from the 6.4 W m^{-2} rms uncertainty in $F_a(0)$ and 12 W m^{-2} uncertainty in $S_a(0)$ are also plotted. The longwave cloud forcing changes by approximately 7 W m^{-2} over the range of SST between 300.25 to 303.25 K. The shortwave cloud forcing decreases by 67 W m^{-2} over the same interval. The corresponding rate of change of $C_s(0)$ with T_s is $dC_s(0)\ /\ dT_s$ = –22 W m^{-2} K^{-1}. Thus the net radiative cooling of the surface by clouds increases by roughly 20 W m^{-2}K^{-1} during the CEPEX observing period. The rate of change of $C_{net}(0)$ is sensitive to the distribution of cold clouds since $C_{net}(0)$ changes by about 3 W m^{-2} for each 1 K change in the median IRBT. The distribution of $\overline{T}_c$ for small regions or for short periods of time may exhibit a different correlation between $\overline{T}_c$ and T_s, and the distribution observed during CEPEX may differ from the climatological mean. However, the increase in convective frequency with SST is a general characteristic of tropical ocean

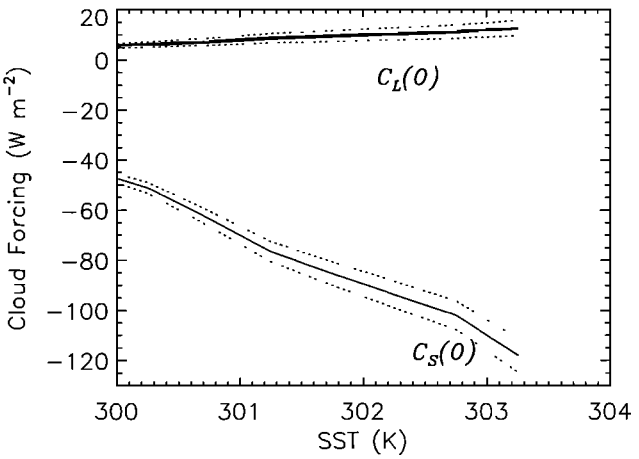

Figure 16. Shortwave and longwave surface cloud forcing estimated by combining *in situ* and satellite data using (24). The brightness temperature distribution used to derive the change in cloud forcing with SST is for the region 20°N to 20°S, 160°E to 160°W between March 7 and April 5, 1993. Dotted lines show 2σ confidence intervals determined from the rms uncertainties in $F_a(0)$ and $S_a(0)$.

regions [*Waliser and Graham*, 1993]. The rate of change of $C_{net}(0)$ is also sensitive to magnitude of $C_s(0)$ for $\overline{T}_c$ greater than 280 K. Most of the surface and low-altitude observations during CEPEX were made under convectively disturbed conditions, which tend to increase the magnitude of $C_s(0)$ and this reduces the rate of change of $C_{net}(0)$ compared to the climatological mean.

5. Discussion and Conclusions

The measurements from the high-altitude ER-2 aircraft have shown that the shortwave and longwave cloud forcing are closely correlated to a radiative measure of the cloud temperature. The net radiative effect of clouds integrated from the surface to the tropopause is much smaller than the individual cloud radiative terms. In contrast to earlier satellite studies, which have demonstrated the cancellation of the longwave and shortwave effects for monthly and seasonal periods [*Ramanathan et al.*, 1989; *Harrison et al.*, 1990], the CEPEX observations show that the cancellation can occur on time scales as short as 1 day. Thus the net radiative heat budget at the tropopause is essentially unchanged by the aggregate effects of clouds associated with deep convection. The heat budget is determined primarily by the sum of the clear-sky shortwave and longwave fluxes, and during the CEPEX observing period the net clear-sky flux across the tropopause is approximately 120 W m^{-2}. The proposed mechanisms for the cancellation involve both cloud physical and microphysical properties [*Kiehl*, 1994; *Jensen et al.*, 1994]. At present it is not clear whether the correlations between physical and microphysical parameters required by these mechanisms can occur sufficiently rapidly to explain the CEPEX measurements. It should be possible to examine the physics of the cancellation in greater detail by using coincident measurements of the parameters from both CEPEX and TOGA COARE.

At the surface the observations indicate that clouds have a large net cooling effect. Because of the infrared opacity and temperature profile of the tropical atmosphere, the longwave cloud forcing at the surface is much smaller than the forcing at the tropopause. The magnitude of the shortwave cloud forcing is strongly correlated with decreasing brightness temperature. In the CEPEX domain the shading effect of trade cumulus cools the surface by approximately 30 W m^{-2}. The largest reductions in surface insolation are observed for clouds extending into the upper troposphere associated with deep convection. The number and fractional area of the cold clouds derived from satellite observations increase with SST, and the fractional area remains near its maximum value above 302 K. The trend in shortwave cloud forcing with SST calculated from the distribution of IRBT with SST and the observed dependence of $C_s(0)$ on IRBT is 22 W m^{-2} K^{-1}. The change in shortwave forcing with SST is larger than the gradient in any other radiative term in the surface energy budget.

The small net forcing at the tropopause implies that the large net cooling at the surface is matched with a nearly equal and opposite diabatic heating in the cloudy troposphere [*Ramanathan et al.*, 1989; *Webster*, 1994]. During CEPEX the radiative diabatic heating due to clouds approaches 100 W m^{-2} when the SST approaches 303 K. The radiative divergence in cloudy regions is comparable to the total diabatic heating of the tropical atmosphere in the central equatorial Pacific [*Hoskins et al.*, 1989; *Siegmund*, 1993; *Trenberth and Solomon*, 1994]. While the vertical profile of cloud forcing has been demonstrated in earlier model calculations, the CEPEX observations provide direct confirmation of its dipole structure and determine the dependence on brightness temperature.

These results may be useful for testing the radiative properties of clouds in atmospheric general circulation models (AGCMs) once calculations of IRBT are added to the model output. Validation of the AGCMs is important for climate studies, since the cloud radiative divergence has significant effects on both the local and large-scale dynamics [e.g., *Slingo and Slingo* 1988; *Sherwood et al.* 1994]. In the past, model simulations of the warm pool have been tuned against satellite measurements of the Earth radiation budget at the top of the atmosphere. The data from CEPEX and TOGA COARE provide the energy budget at both the surface and TOA as well as the changes in the radiative and nonradiative components with convective activity. These observations represent a new and stringent data set for testing the parameterization of convection and radiative transfer in AGCMs.

Acknowledgments. This research was supported by grants NSF ATM89-20119 (W.D.C. and D.L.), NSF ATM94-13294 (P.J.F.), NSF ATM92-23467 (F.P.J.V. and P.P.) and DOE DE-FG03-91ER61198 (D.L.) and with funding from Westgec (P.J.F.) and the Ministry for Research and Technology of the Federal Republic of Germany (H.G.). CEPEX was funded by NSF and DOE. J. D. Spinhirne and W. D. Hart generously provided their analysis of the vertical distribution of clouds from the lidar on the NASA ER-2. We would like to thank S. K. Cox and E. Dutton for letting us use their calibration instruments. We would also like to thank the entire crew of the R/V *Vickers*, as well as U. Schmid and W. Biselli for launching the radiosondes and maintaining the surface observations from the ship. The NOAA P-3 radiometers were calibrated by G. Kumor using facilities at the University of Hawaii through the generous assistance of D. Stevens. The gridded fields of SST were provided by the ECMWF. The suggestions and recommendations of D. Hartmann and one anonymous referee are gratefully acknowledged. This paper is report 135 from the Center for Clouds, Chemistry, and Climate (C^4)

References

Anderson, E. R., Energy budget studies, *U S. Geol Surv. Circ.*, *229*, 71-119, 1952.

Barkstrom, B. R., The Earth Radiation Budget Experiment (ERBE), *Bull. Am. Meteorol. Soc.*, *65*, 1170-1185, 1984.

Barkstrom, B. R , and G. L. Smith, The Earth Radiation Budget Experiment· Science and implementation, *Rev. Geophys.*, *24*, 379-390, 1986.

Brooks, D. R , E. F. Harrison, P. Minnis, and J. T. Suttles, Development of algorithms for understanding the temporal and spatial variability of the Earth's radiation balance, *Rev. Geophys*, *24*, 422-438, 1986.

Cess, R. D., and G. L. Potter, Exploratory studies of cloud radiative forcing with a general circulation model, *Tellus*, *39A*, 460-473, 1987.

Cess, R. D., E. F. Harrison, P. Minnis, B. R. Barkstrom, V. Ramanathan, and T. Y. Kwon, Interpretation of seasonal cloud-climate interactions using Earth Radiation Budget Experiment data, *J. Geophys. Res.*, *97*, 7613-7617, 1992.

Cess, R. D., et al, Absorption of solar radiation by clouds: Observations versus models, *Science*, *267*, 496-499, 1995.

Charlock, T. P., and V. Ramanathan, The albedo field and cloud radiative forcing produced by a general circulation model with internally generated cloud optics, *J. Atmos. Sci.*, *42*, 1408-1429, 1985.

Fouquart, Y., J. C. Buriez, and M. Herman, The influence of clouds on radiation: A climate-modeling perspective, *Rev. Geophys.*, *28*, 145-166, 1990.

Gupta, S. K., W. F. Staylor, W. L. Darnell, A. C. Wilber, and N. A. Ritchey, Seasonal variation of surface and atmospheric cloud radiative forcing over the globe derived from satellite data, *J. Geophys. Res.*, *98*, 20,761-20,778, 1993.

Harrison, E. F., P. Minnis, B. R. Barkstrom, V. Ramanathan, R. D. Cess, and G. G. Gibson, Seasonal variation of cloud radiative forcing derived from the Earth Radiation Budget Experiment, *J. Geophys. Res*, *95*, 18,687-18,703, 1990.

Harshvardhan, D. A. Randall, and D. A. Dazlich, Relationship between the longwave cloud radiative forcing at the surface and the top of the atmosphere, *J. Clim.*, *3*, 1435-1443, 1990.

Hartmann, D. L., and M. L. Michelsen, Large-scale effects on the regulation of tropical sea surface temperature, *J. Clim.*, *6*, 2049-2062, 1993.

Hartmann, D. L., V. Ramanathan, A. Berroir, and G E Hunt, Earth radia-

tion budget data and climate research, *Rev. Geophys., 24*, 439-468, 1986.

Haskins, R. D., T. P. Barnett, M. M. Tyree, and E. Roeckner, Comparison of cloud fields from AGCM, *in situ*, and satellite measurements, *J. Geophys. Res., 100*, 1367-1378, 1995.

Heymsfield, A. J., and R. M. Sabin, Cirrus crystal nucleation by homogeneous freezing of solution droplets, *J. Atmos. Sci., 46*, 2252-2264, 1989.

Hoskins, B. J., H. H. Hsu, I. N. James, M. Masutani, P. D. Sardeshmukh, and G. H. White, Diagnostics of the global atmospheric circulation based on ECMWF analyses 1979-1989, Tech. Rep., *WMO/TD-326*, World Meteorological Organization, Geneva, 1989. (Also available as *WMO/TD-27*, World Clim. Res. Program, Geneva, 1989.)

Inamdar, A. K., and V. Ramanathan, Physics of greenhouse effect and convection in warm oceans, *J. Clim., 7*, 715-731, 1994.

Jensen, E. J., S. Kinne, and O. B. Toon, Tropical cirrus cloud radiative forcing: Sensitivity studies, *Geophys. Res. Lett., 21*, 2023-2026, 1994.

Kiehl, J. T., On the observed near cancellation between longwave and shortwave cloud forcing in tropical regions, *J. Clim., 7*, 559-565, 1994.

Kiehl, J. T., and V. Ramanathan, Comparison of cloud forcing derived from the Earth Radiation Budget Experiment with that simulated by the NCAR Community Climate Model, *J. Geophys. Res., 95*, 11,679-11,698, 1990.

Lau, K. M., C. H. Sui, M. D. Chou, and W. K. Tao, An inquiry into the cirrus-cloud thermostat effect for tropical sea surface temperature, *Geophys. Res. Lett., 21*, 1157-1160, 1994.

Li, Z., and L. Garand, Estimation of surface albedo from space: A parameterization for global application, *J. Geophys. Res., 99*, 8335-8350, 1994.

Li, Z., and H. G. Leighton, Estimation of SW flux absorbed at the surface from TOA reflected flux, *J. Clim., 6*, 317-330, 1993.

Lubin, D., D. Cutchin, W. Conant, H. Grassl, U. Schmid, and W. Biselli, Spectral longwave emission in tropics: FTIR measurement at the sea surface and comparison with fast radiation codes, *J. Clim., 8*, 286-295, 1995.

Michalsky, J. J., The *Astronomical Almanac's* algorithm for approximate solar position (1950-2050), *Sol. Energy, 40*, 227-235, 1988.

Murayama, N., *The GMS Users' Guide*, Tokyo, 2nd ed., Meteorol. Satell. Cent., 1989.

Ockert-Bell, M. E., and D. L. Hartmann, The effect of cloud type on Earth's energy balance: Results for selected regions, *J. Clim., 5*, 1157-1171, 1992.

Payne, R. E., Albedo of the sea surface, J. Atmos. Sci., *29*, 959-970, 1972.

Pilewskie, P., and F. P. J. Valero, Direct observation of excess solar absorption by clouds, *Science, 267*, 1626-1629, 1995.

Ramanathan, V., Interactions between ice-albedo, lapse-rate and cloud-top feedbacks: An analysis of the nonlinear response of a GCM climate model, *J. Atmos. Sci., 34*, 1885-1897, 1977.

Ramanathan, V., The role of Earth radiation budget studies in climate and general circulation research, *J. Geophys. Res., 92*, 4075-4095, 1987.

Ramanathan, V., and W. Collins, Thermodynamic regulation of ocean warming by cirrus clouds deduced from observations of the 1987 El Niño, *Nature, 351*, 27-32, 1991.

Ramanathan, V., R. D. Cess, E. F. Harrison, P. Minnis, B. R. Barkstrom, E. Ahmad, and D. Hartmann, Cloud-radiative forcing and climate: Results from the Earth Radiation Budget Experiment, *Science, 243*, 57-63, 1989.

Ramanathan, V., R. Dirks, R. Grossman, A. Heymsfield, J. Kuettner, and F.P.J. Valero, *Central Equatorial Pacific Experiment Design*. Center for Clouds, Chemistry, and Climate, Univ. of Calif., San Diego, 1993.

Ramanathan, V., W. D. Collins, and B. Subasilar, Comment on "An inquiry into the cirrus-cloud thermostat effect for tropical sea surface temperature" by K. M. Lau, C. H. Sui, M. D. Chou and W. K. Tao, *Geophys. Res. Lett., 21*, 1185-1186, 1994.

Ramanathan, V., B. Subasilar, G. Zhang, W. Conant, R. Cess, J. Kiehl, H. Grassl, and L. Shi, Warm pool heat budget and shortwave cloud forcing: A missing physics?, *Science, 267*, 499-502, 1995.

Raval, A., and V. Ramanathan, Observational determination of the greenhouse effect, *Nature, 342*, 758-761, 1989.

Rossow, W. B., Y. Desormeaux, C. L. Brest, and A. Walker, International Satellite Cloud Climatology Project (ISCCP): Radiance calibration report. Technical Report, NASA Goddard Inst. for Space Stud., New York, 1992.

Sherwood, S. C., V. Ramanathan, T. P. Barnett, M. K. Tyree, and E. Roeckner, Response of an atmospheric GCM to radiative forcing of tropical clouds, *J. Geophys. Res., 99*, 20,829-20,845, 1994.

Siegmund, P., Cloud diabatic forcing of the atmosphere, estimated from simultaneous ECMWF diabatic heating and ISCCP cloud amount observations, *J. Clim., 6*, 2419-2433, 1993.

Slingo, A., and J. M. Slingo, The response of a general circulation model to cloud longwave radiative forcing, I, Introduction and initial experiment, *Q. J. R. Meteorol. Soc., 114*, 1027-1062, 1988.

Spencer, J. W., Comments on *Astronomical Almanac's* algorithm for approximate solar position (1950-2050), *Sol. Energy, 42*, 353, 1989.

Spinhirne, J. D., and W. D. Hart, Cirrus structure and radiative parameters from airborne lidar and spectral radiometer observations: The 28 October 1986 FIRE study, *Mon. Weather Rev., 118*, 2329-2343, 1990.

Stephens, G. L., and S.-C. Tsay, On the cloud absorption anomaly, *Q. J. R. Meteorol. Soc., 116*, 671-704, 1991.

Stephens, G. L., and P. J. Webster, Cloud decoupling of the surface and planetary radiative budgets, *J. Atmos. Sci., 41*, 681-686, 1984.

Suttles, J. T., Angular radiation models for Earth-atmosphere system: Technical report, *NASA Ref. Publ. 1184*, 1988.

Trenberth, K. E., and A. Solomon, The global heat balance: Heat transports in the atmosphere and ocean, *Clim. Dyn., 10*, 107-134, 1994.

Valero, F. P. J., W. J. Y. Gore, and L. P. M. Giver, Radiative flux measurements in the troposphere, *Appl. Opt., 21*, 831-838, 1982.

Valero, F. P. J., T. P. Ackerman, and W. J. Y. Gore, The absorption of solar radiation by the Arctic atmosphere during the haze season and its effects on the radiation budget, *Geophys. Res. Lett., 11*, 465-468, 1984

van de Hulst, H. C., *Light Scattering by Small Particles*. 447 pp., Dover, Mineola, N.Y., 1981.

Waliser, D. E., and N. E. Graham, Convective cloud systems and warm-pool sea surface temperatures: Coupled interactions and self-regulation, *J. Geophys. Res, 98*, 12,881-12,893, 1993.

Weaver, C. P., W. D. Collins, and H. Grassl, The relationship between clear-sky atmospheric greenhouse effect and deep convection during the Central Equatorial Pacific Experiment (CEPEX): Model calculations and satellite observations, *J. Geophys. Res., 99*, 25,891- 25,901, 1994.

Webster, P. J., The role of hydrological processes in ocean-atmosphere interactions, *Rev. Geophys., 32*, 427-476, 1994.

Webster, P. J., and R. Lukas, TOGA COARE: The Coupled Ocean Atmosphere Response Experiment, *Bull. Am. Meteorol Soc., 73*, 1377-1416, 1992.

Webster, P. J., and G. L. Stephens, Cloud-radiation interactions and the climate problem, in *The Global Climate*, edited by J. Houghton, pp. 63-78, Cambridge Univ. Press, New York, 1984.

Wielicki, B. A., and L. Parker, On the determination of cloud cover from satellite sensors: The effect of sensor spatial resolution, *J. Geophys. Res., 97*, 12,799-12,823, 1992.

Williams, S. F., *Central Equatorial Pacific Experiment (CEPEX) Operations Summary*. Office of Field Proj. Support, Univ. Corp. for Atmos. Res., Boulder, Col., 1993.

Young, G. S., D. V. Ledvina, and C. W. Fairall, Influence of precipitating convection on the surface energy budget observed during a Tropical Ocean Global Atmosphere pilot cruise in the tropical western Pacific ocean, *J. Geophys. Res., 97*, 9595-9603, 1992.

Zhang, C., Large scale variability of atmospheric deep convection in relation to sea surface temperature in the tropics, *J. Clim., 6*, 1898-1913, 1993.

W.D. Collins, F.P.J. Valero, P.J. Flatau, and D. Lubin, Scripps Institution of Oceanography, 9500 Gilman Drive, MC 0221, University of California, La Jolla, CA. 92093-0221. (email: wcollins@ucsd.edu; fvalero@ucsd.edul; pflatau@ucsd.edu; dlubin@ucsd.edu)

H. Grassl, World Climate Research Programme, World Meteorological Organization, Case Postale 2300, CH-1211 Geneva 2, SWITZERLAND. (email: grassl@wcrp2.wmo.ch)

P. Pilewskie, NASA Ames Research Center, MS 245-4, Moffett Field, CA. 94035-1000. (email: pil@ra.arc.nasa.gov)

(Received April 4, 1995; revised August 4, 1995, accepted August 7, 1995.)